International Journal of Heat and Mass Transfer 93 (2016) 500–512

Contents lists available at ScienceDirect

International Journal of Heat and Mass Transfer

journal homepage: www.elsevier.com/locate/ijhmt

Heat transfer correlation between Molten Salts and helical-coil tube bundle Steam Generator

Esther Rivas *, Esther Rojas

CSSU-Thermal Storage, CIEMAT-PSA, Av. Complutense 40, 28040 Madrid, Spain

ARTICLE INFO

Article history:
Received 20 January 2015
Received in revised form 10 September 2015
Accepted 6 October 2015
Available online 11 November 2015

Keywords:
Concentrating Solar Power (CSP)
Thermal Energy Storage system with integrated Steam Generator (TES-SG)
Molten Salts (MS)
Helical-coil tube bundle
Heat transfer coefficient
Computational Fluid Dynamic (CFD)

ABSTRACT

A Computational Fluid Dynamic (CFD) modelling able to describe a discharge process of a Molten Salts (MS) Thermal Energy Storage system with integrated Steam Generator (TES-SG) is presented in this paper. This simulation model has been validated with experimental results obtained at the PCS Facility located at the ENEA Casaccia Research Centre in Rome. The numerical results of this model (MS velocities, temperatures and boundary heat flux distributions within the SG) have been used to derive a dimensionless form for describing fluid flow, by Reynolds number, Re, and heat transfer between MS and helical-coil tube bundle SG, by Nusselt number, Nu. The obtained correlation is: $Nu = 0.3146Re^{0.54}Pr^{0.36}$, where Re and Nu are based on the outer diameter of the helical coils. It is valid for 400 to 1200 Reynolds numbers, 4 to 11 Prandtl numbers, an average winding angle of 2° and an outer diameter of the helical coils of 0.0127 m. The correlation here proposed can be very useful for sizing a vertical helical-coil tube bundle SG immersed in a Molten Salts tank of a commercial CSP plant for a specific nominal power.

1. Introduction

Thermal Energy Storage (TES) systems are an added value for Concentrating Solar Power (CSP) technologies since they buffer the transient weather conditions, improve their dispatchability, increase their annual capacity factor and allow a more even distribution of electricity production [1,2]. The objective of OPTS project (Optimization of a Thermal Energy Storage system with integrated Steam Generator, 2011–2014, FP7 funded project under 283138 Contract) has been to provide the efficient and techno-economic viability of a new TES concept for the next CSP plants generation, based on:

- The use of Molten Salts (MS) as heat transfer fluid & storage medium.
- The use of a single tank (or thermocline tank) instead of the traditional two-tank configuration.
- The integration of the Steam Generator (SG) that feeds the power block within the storage tank.

One of the OPTS tasks aimed at estimating heat transfer correlations needed for the simulation of a helical-coil tube bundle SG in contact with MS, under defined working conditions on the water-steam side and natural or assisted convection on the MS side. The scope of this paper is the heat transfer in the MS side, since the correlations found in the literature for helical-coil tube bundles [3–5] are not adequate for the OPTS configuration because, they are either not suitable for MS as heat transfer medium or the heat exchanger designs are different enough to influence the heat transfer process.

For this purpose, a Computational Fluid Dynamic (CFD) model of the $300kW_{th}$ MS prototype erected in the Casaccia Research Centre of ENEA (Italy) has been carried out, which has been validated with the experimental data obtained during one of its discharge tests.

The advantage of CFD techniques is to contribute with a detailed description of the thermo-hydraulic behaviour of systems. In the ENEA prototype at issue, these simulations have been able to

Abbreviations: CFD, Computational Fluid Dynamical; MS, Molten Salts; TES-SG, Thermal Energy Storage system with integrated Steam Generator; PCS, Prova Colletori Solari; ENEA, Agenzia nazionale per le nuove tecnologie, l'energia e lo sviluppo economico sostenibile; SG, Steam Generator; TES, Thermal Energy Storage; CSP, Concentrating Solar Power; OPTS, Optimization of a Thermal Energy Storage system with integrated Steam Generator; OECD, Organisation for Economic Co-operation and Development; CAD, Computer Aided Design; SIMPLE, Semi-Implicit Method for Pressure Linked Equations; RANS, Reynolds-Average Navier–Stokes; K–E, K–epsilon; CIEMAT, Centro de Investigaciones Energéticas, Medioambientales y Tecnológicas; UDF, User Defined Function; CPU, Central Processing Unit; UTRINN-STD, Technical Unit for Renewable Energy Sources-Solar Thermodynamic Laboratory; MAPE, Mean Absolute Percentage Error; MADP, Mean Absolute Deviation Percent.

* Corresponding author. Tel.: +34 91 4962513.
E-mail address: esther.rivas@ciemat.es (E. Rivas).

http://dx.doi.org/10.1016/j.ijheatmasstransfer.2015.10.013
0017-9310/

Nomenclature

Re	Reynolds number
Nu	Nusselt number
d_o	outer diameter
d_h	hydraulic diameter
Δs	cell size
Δt	time step
Pr_T	turbulent Prandtl number
Pr	molecular Prandtl number
f_g	buoyancy force
C_p	heat capacity
$\overline{Cp}$	average heat capacity
$\dot{Q}$	power
$\dot{m}$	mass flow rate
H	enthalpy
T	temperature
h	heat transfer coefficient
$\bar{h}$	local heat transfer coefficient
ΔS	surface element
v	velocity

Greek symbols

ρ	density
β	thermal expansion coefficient
κ	thermal conductivity
μ	dynamic viscosity

Subscripts

m	mth helical turn
n	nth helical turn in a uniformly distributed subset of them
MS	molten salts
WS	water steam
OUT	outlet condition
IN	inlet condition
∞	bulk
w	wall

provide the MS velocities, temperatures and boundary heat flux distributions within the SG needed to explain the heat transfer in the MS. This kind of information cannot be obtained by means of more simplified simulations [6], neither examining prototype experimental data [7].

The commercial code STAR-CCM+8.04.010® (based on finite volume method [8]) has been used as CFD tool.

The conducted layout is as follows: in the next section, a literature survey of heat transfer correlations for helical-coil tube bundles is presented. In Section 3, the ENEA prototype is introduced and in Section 4 the CFD model that describes the MS behaviour during its discharge is described, both the pre-processing – establishing the geometry, meshing, and simulation model – as the processing. In Section 5 the model is validated in terms of both numerical parameters and experimental data. From the numerical results, in Section 6 a methodology for calculating the local heat transfer coefficients along the SG is established and in Section 7, these coefficients are linked with representative dimensionless numbers, so a new heat transfer correlation for MS is proposed and discussed. In the last section, the main conclusions of the study are included.

2. Literature survey of heat transfer correlations for helical-coil tube bundles

Studies on convective heat transfer in helical coil heat exchangers on the shell-side are scarce in the literature and the reported configurations are limited to very specific situations and configurations. Messa et al. [3], proposed several heat transfer correlations founded on an experimental work with six different kind of helical coil heat exchangers of winding angles from 4° 30′ up to 18° 30'. Smith [4], carried out a thermal design using the data of one OECD Dragon helium-steam heat exchanger. Abadzic [4], examined the heat transfer data from different sources and recommended three correlations for an extended range of Reynolds numbers, *Re*. Most of the data correlated correspond to non-uniform helical-coil bundles with mean winding angles of 9°. Geníc et al. [5], have recently presented a new correlation founded on an experimental research with three helical heat exchangers of different winding angles (from 4° 26′ up to 42° 28′). The first correlations are based on the outer diameter, d_o, and the last in the hydraulic diameter, d_h.

He et al. [31], studied convective heat transfer of MS around a tube bundle, proposing a correlation valid for Prandtl numbers, *Pr*, between 20 to 100 and 0.0432 m hydraulic diameter, d_h.

In the following table, Table 1, correlations mentioned in the previous works are summarized.

Smith's and Abadzic's correlations are only suitable for gases ($Pr \sim 1$) and Messa et al.'s (1), (3), (4), (5) and (6) are suitable for gases and liquids with low *Pr* number (up to 2.6).

He et al.'s correlation, that, despite it is suitable for MS, the heat exchanger configuration for which was validated (a common tube bundle) is less effective in transferring heat that the helical-coil tube bundle configuration.

3. ENEA prototype

The TES-SG prototype is based on a joint patent between the company Ansaldo Nucleare S.p.A (Italy) and ENEA Research Centre (Italy), [9].

It is a stainless steel tank, of nearly 2 m diameter and 2.8 m height covered by an insulating layer, which contain 12,000 kg of molten solar salt (60% weight $NaNO_3$ + 40% weight KNO_3).

SG is integrated vertically at one side of the tank and is composed by three concentric and uniform helical coils (of 65 helical turns), an insulating blanket around them, a downcomer in their core and an opening and a diffuser through which the MS enter and leave the SG respectively (Fig. 1, [10]).

During TES discharge, saturated water goes through the Steam Generator, along the downcomer and is distributed through the three helical coils that are born at the end of the downcomer. Along these three helical coils MS exchange their energy with the water flowing up to the helical coils, becoming steam and inducing a self-sustaining flow by natural convection in the MS side.

This process causes the stratification in the Molten Salts bulk (outside the SG), i.e., originates the appearance of a cold zone at the bottom of the tank, from the MS which have flowed through the SG exchanging heat, a hot zone at the top of the tank, and an intermediate zone between them. As discharge progresses the bulk MS stratification changes.

The 300kW_{th} ENEA prototype has different temperature gauges (TI.), placed in the physical media (MS, water-steam and air) and at various positions of walls (tank, SG shell, central helical coil);

Table 1
Reported correlations on convective heat transfer in helical-coil heat exchangers on the shell-side and MS in tube bundles.

Ref.	Relative correlation number	Correlation	*Re*
[3]	(1)	$Nu_{d_0} = 0.0567Re^{0.71}Pr^{0.93}$	500–45,000
	(2)	$Nu_{d_0} = 0.0085Re^{0.84}Pr^{0.57}$	900–7500
	(3)	$Nu_{d_0} = 0.0305Re^{0.85}Pr^{0.70}$	400–7500
	(4)	$Nu_{d_0} = 0.0320Re^{0.83}Pr^{1.14}$	800–12,000
	(5)	$Nu_{d_0} = 0.0851Re^{0.71}Pr^{1.02}$	400–37,000
	(6)	$Nu_{d_0} = 0.0214Re^{0.86}Pr^{0.83}$	500–7000
[4]		$Nu_{d_0} = 0.063235Re^{0.794}Pr^{0.36}$	1000–10,000
[4]	(1)	$Nu_{d_0} = 0.0567Re^{0.71}Pr^{0.93}$	1000–20,000
	(2)	$Nu_{d_0} = 0.0567Re^{0.71}Pr^{0.93}$	20,000–200,000
	(3)	$Nu_{d_0} = 0.0567Re^{0.71}Pr^{0.93}$	200,000–900,000
[5]		$Nu_{d_h} = 0.50Re^{0.55}Pr^{0.33}\left(\frac{\mu}{\mu_w}\right)^{0.14}$	1000–9000
[31]		$Nu_{d_h} = 1.61\left(\frac{RePr}{l/d_h}\right)^{0.63}\left(\frac{\mu}{\mu_w}\right)^{0.14}$	400–2300

pressure gauges (PI.), at the water inlet and outlet; and volumetric flow gauges (FI.) at the SG inlet (before the downcomer) and at the inlet of every helical coil (at the end of the downcomer). Differential pressure (ΔPI.) between the inlet and outlet of every helical coil is measured by calibrated orifices.

These experimental data will be used to stablish initial and boundary conditions of the CFD model, validate its results and identify the steady state in the water-steam side during discharge where local heat transfer coefficients of MS will be calculated.

4. CFD model

4.1. Geometry

A 3D full-scale geometric modelling including both the immersed SG and the whole tank has been erected (global model). Thus, the movement of the MS both in the tank and through the SG can be studied simultaneously, and therefore, how the heat transfer within the SG influences the time-evolution of bulk MS stratification during discharge.

Erecting a global model has been chosen to avoid guessing a velocity profile coming to the SG and to count with more experimental data to validate the CFD model.

CAD 3D software Inventor® 2010 has been used to build the three helical coils of the SG while CAD module of STAR-CCM +8.04.010® has been used to build the rest of the components of the SG (insulating blanket, downcomer, opening and diffuser, Fig. 2), and the tank.

It has been assumed that the walls of the diffuser and the opening of the SG have negligible thickness, but a thermal resistance of $1.562 \cdot 10^{-4}$ m^{2}K/W (equivalent to a 0.0025 m thickness AISI 321H wall with thermal conductivity 16 W/mK). The insulating blanket is also considered to have a negligible thickness.

4.2. Mesh

The domain has been divided into different subdomains, subdomains 0, 1, 2 and 3 in Fig. 3, which have been discretized with a polyhedral cells mesh. The maximum size of such cells (Δs) is

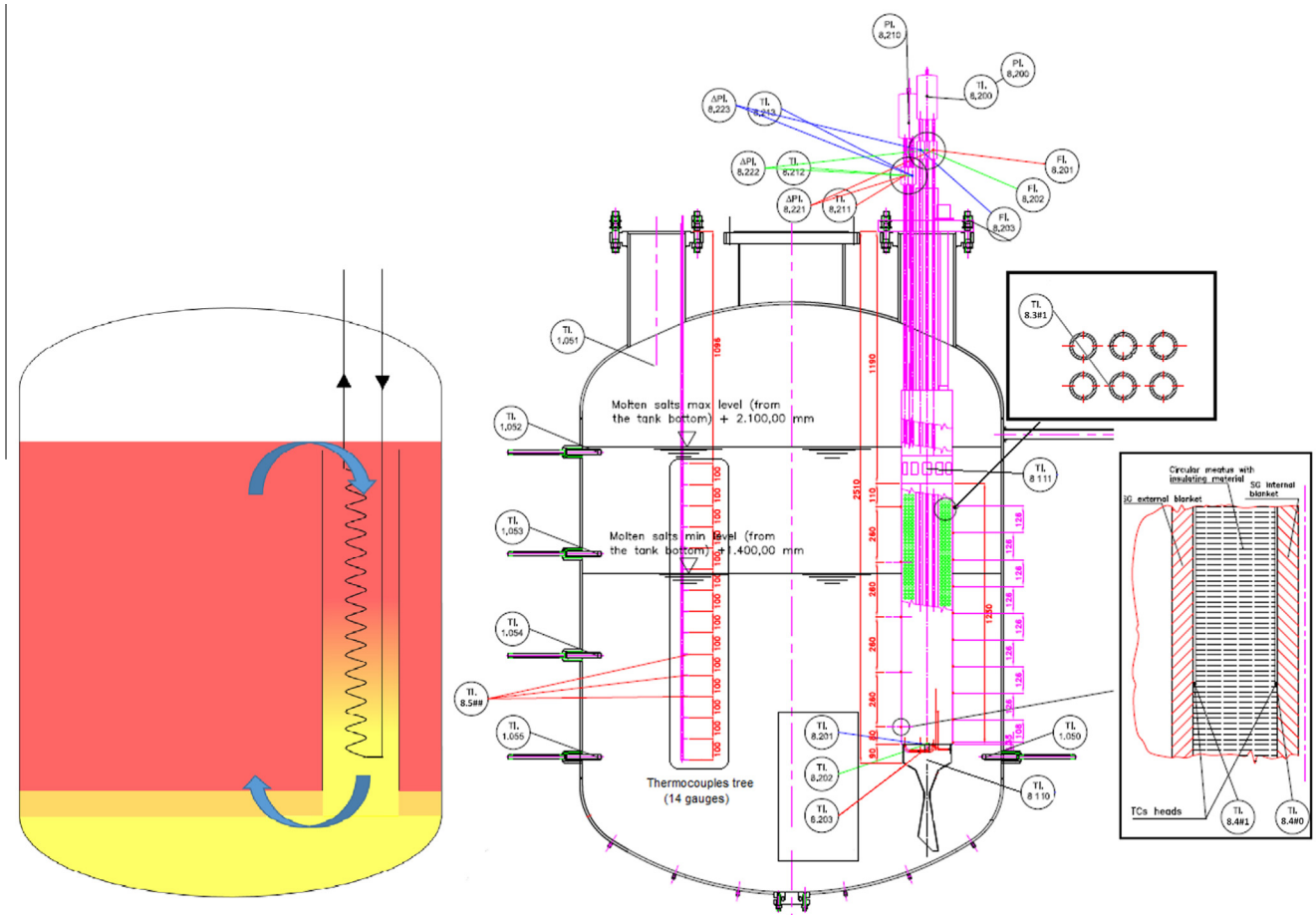

Fig. 1. Scheme of the TES-SG prototype in Casaccia (Rome) [10].

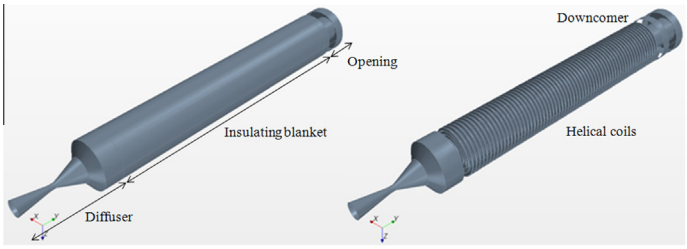

Fig. 2. External and internal perspective views of the SG.

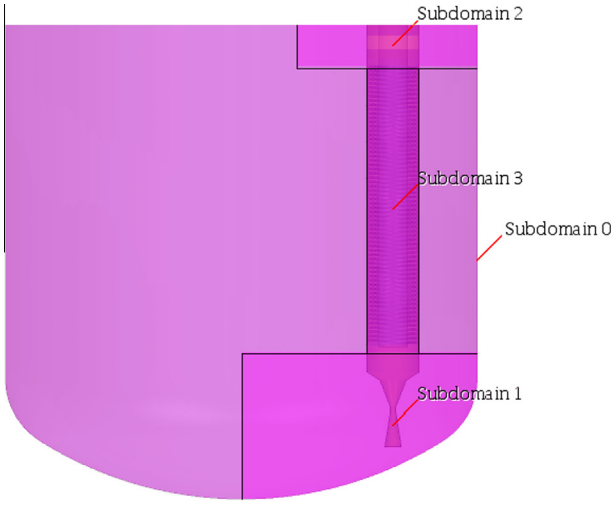

Fig. 3. Subdomains for the meshing.

0.05 m in subdomain 0 (corresponding to the MS of the tank bulk), 0.005 m in subdomain 3 (corresponding to the MS within the SG) and 0.025 m in subdomains 1 and 2 (corresponding to the MS around the opening and diffuser of the SG). Boundary prism layers with a 0.0025 m (SG) and 0.0250 m (tank) maximum size have been created. Differences in cell sizes are necessary for optimising computational time without losing any relevant physical phenomena.

The automatic meshing module of STAR-CCM+8.04.010® has been used. The total number of cells used has been approximately $1.675 \cdot 10^6$, among which about 84% belongs to the SG.

Passing from the minimum to maximum cell sizes has been done gradually. As examples, in Fig. 4 four detailed views of meshing in a cross-section along SG axis are shown. There it can be seen a soft transition from 0.05 m in the bulk of the tank to 0.005 m in the bulk of the SG (Fig. 4(a)), refinements around helical coils (Fig. 4(b)) as well as the soft transition at the SG inlet and outlet (Fig. 4(c) and (d)).

The parameters available in STAR-CCM+ to determine the overall quality of the volume mesh are: *cell and boundary skewness angles*, *face validity metric*, *cell quality metric* and *volume change metric* [8]. The *skewness* measures are designed to reflect whether the cells on either side of a face are formed in such a way as to permit diffusion of quantities without these quantities becoming unbounded. *Skewness angles* of 90° or greater, typically result in solver convergence issues. The *face validity* is an area weighted measure of the correctness of the face normal relative to their attached cell centroid. Values of below 0.5 signify a negative volume cell. The *cell quality metric* is a function not only of the relative geometric distribution of the cell centroids of the face neighbour cells, but also of the orientation of the cell faces. A degenerate cell has a *cell quality* approaching zero. The *volume change metric* describes the ratio of the volume of a cell to that of its largest neighbours. Cells with a *volume change* value of $1 \cdot 10^{-5}$ or below should be investigated.

In the next table, Table 2, the results of mesh diagnostic are shown

Considering the limiting values of the previous parameters, it could be said that the quality of the volume mesh is suitable.

4.3. Modelling

The system to model is a quasi-isolated system with an energy sink inside (the SG) and, therefore, its thermo-hydraulic behaviour is intrinsically unsteady, i.e., dependent on time.

An *implicit formulation* has been used since it is the suitable for incompressible flows. This method calculates the solution by solving the set of equations by iteration with time[1]. The *Segregated Flow model* has been chosen because fits well for natural convection cases involving low Rayleigh numbers. It uses less memory than the coupled algorithm but the number of iterations required increases with mesh size. Flow equations are solved in a segregated or uncoupled manner (one for each component of velocity, and one for pressure).

The linkage between the momentum and mass conservation equations is achieved with a predictor–corrector approach. The complete formulation can be described using a collocating variable arrangement and a Rhie and Chow pressure–velocity coupling [11–16] combined with a SIMPLE type algorithm [17].

The *Segregated Fluid Temperature model* has been adopted to solve the total energy equation. In this, the temperature is the unknown variable and the enthalpy is computed from the temperature according to the equation state.

Besides, the following approaches have been considered:

- A *turbulence model* for the viscous regime since, even though in the tank bulk the movement is "ordered", within the SG the circulation is complex.
- A *Reynolds-Average Navier–Stokes (RANS) approach* (based on the concept of Reynolds averaging) to modelling the turbulence. It is the most reliable for the prediction of turbulent flows since it is validated for a wide field of applications (as can be seen in [18–20]: three very different examples of induced flows by natural convection).

These models form the basis of standard turbulence calculation procedures in currently available commercial CFD codes.

- Closing the RANS equations is made with the *Realizable K–E Two-Layer model* considering the optional *Two-Layer Xu formulation* ([21]) (specifically developed for natural convection) and the flexibility of the *all Y+* wall hybrid treatment.

[1] In opposition with explicit methods that compute, directly, the dependent variables in terms of known quantities in the previous time.

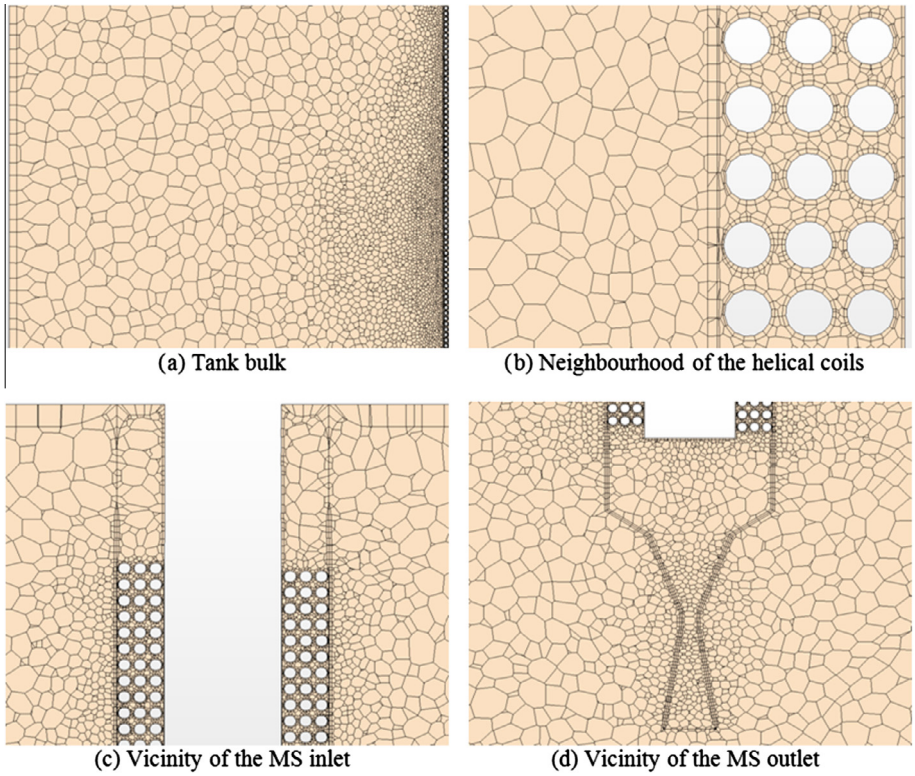

Fig. 4. Detailed views of meshing.

Table 2
Mesh diagnostic.

Parameter	Minimum value	Maximum value
Cell and boundary skewness angles	0°	81°
Face validity	1	1
Cell quality	0.05	0.98
Volume change	0.007	1

The K–E models provide a good compromise between robustness, computational cost and accuracy.

These models need to be accompanied by a wall treatment to solve the transition between the viscous sub-layer and the logarithmic layer. The all Y+ is a hybrid wall treatment based on blended laws. These laws address the transition as a separate region and are adequate when the mesh has a medium resolution.

For the free parameters of the turbulent model, here it has been used the default values of STAR-CCM+8.04.010®.

Another free parameter of the turbulent model that is needed is the turbulent Prandtl number, Pr_T, which is defined as the ratio between the momentum eddy diffusivity and the heat transfer eddy diffusivity. The MS are characterised by a high molecular Prandtl number, Pr, therefore their heat transfer characteristics are slightly affected by the specific value of Pr_T, as it is extensively supported by Jischa and Rieke [22]. Churchill's correlation, [23], has been used to calculate Pr_T,

$$Pr_T = 0.85 + \frac{0.015}{Pr}$$

- *Boussinesq approximation* has been applied since the density variations with the temperature are considered small enough in the range of operating conditions $\left(\left|\frac{\rho_{max}-\rho_{min}}{\rho_{max}}\right| \ll 1\right)$, as to assume a constant density (ρ_{min}) in all the momentum terms except in the buoyancy force term ($f_g = g\rho_{min}\beta_{min}\Delta T$).
- Thermo-physical properties of MS -heat capacity (C_p), thermal conductivity (κ) and dynamic viscosity (μ)- are considered dependant on temperature, like Bradshaw and Carling, [24], and Ferri et al., [25], propose.

4.3.1. Initial and boundary conditions

Since the validation of the model with experimental data will be done using the data set of October, 29th 2012 test, [7], the initial and boundary conditions are defined accordingly. In Fig. 5, the water side working conditions during the test are shown. These are the total water volumetric flow rate measured before going into the SG (FI.7002), water temperature at the downcomer inlet (TI.8.200 in Fig. 1), water temperatures at the SG coils inlets (TI.8.20#, where # may be 1, 2, 3, in Fig. 1), steam temperatures at the coils outlet (TI.8.21#, where # may be 1, 2, 3, in Fig. 1), water pressure at the downcomer inlet (PI.8.200, in Fig. 1) and steam pressure at the SG outlet (PI.8.210, in Fig. 1).

The water loop follows a transient state, in red (1650–5250 s), then a steady state, in green (5250–11,350 s) and, finally, another transient state, in red (11,350–12,050 s). The simulation start time has been set up at the beginning of the first transient state, i.e., at the beginning of the discharge (1650 s real time) and continues through the transient and the steady states of water-steam side until 7050 s real time.

Regarding to the initial conditions, MS and helical coils are assumed to be at 483 °C, [7].

The tank wall, the MS-air interface, SG insulating blanket and downcomer are assumed to be adiabatic boundaries. These assumptions are based not only on system design (insulating layer of 0.4 m covering the tank and SG insulating blanket of 0.014 m) but also on a previous experimental data analysis of prototype, [7], where it was observed that the temperatures at these surfaces were the same as their surrounding MS.

The main boundary conditions imposed are the temperature profiles along time in the three helical coils. Time averages of

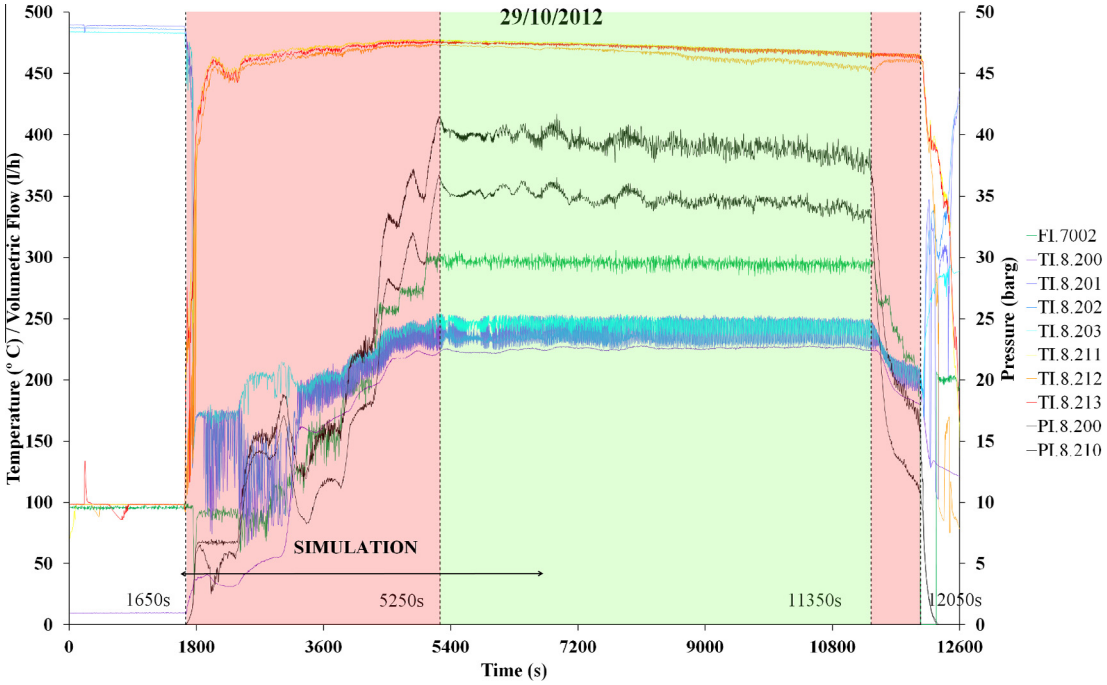

Fig. 5. Some data set for 29th October 2012 test [7].

experimental helical coil temperatures every 20 min have been done in order to reduce the observed fluctuations. As pointed out by Rivas and Rojas, [7], these fluctuations do not have mayor effects on the time-evolution MS bulk temperatures.

Since these experimental data have been recorded only every 7 helical turns and for the simulation every helical turn has to be given a temperature profile, first, the averaged values have been fitted to continuous functions of type logistic-CFD (Fig. 6),

$$T_t(T_{max}, T_{min}, H_0, s) = T_{max} + \frac{T_{min} - T_{max}}{1 + e^{\left(\frac{H - H_0}{s}\right)}}$$

where T_{max}, T_{min}, H_0 and s are their characteristic parameters which are different for each time t (Table 3).

And then, based on these continuous functions, a table $\{x, y, z, T_{0\,s}, T_{1200\,s}, T_{2400\,s}, T_{3600\,s}, T_{4800\,s}, T_{6000\,s}, T_{7200\,s}, T_{8400\,s}, T_{9345\,s}\}$ has been built assuming a fit by splines for coil temperature profiles with time since the errors made in the process are lower than when using a fit by steps or linear. The three helical coils are assumed to have the same temperature profiles (Fig. 7).

4.4. Model processing

Regarding the discretization of the governing equations, a second order upwind scheme has been adopted for momentum, turbulence kinetic energy, turbulence dissipation rate and energy equations, while a first order scheme has been used to the temporal discretization.

The simulation has been run on 16 nodes Intel(R) Xeon(R) CPU E5450 @ 3.0 GHz, of 8 cores each one, belonging to the CIEMAT's cluster named Euler.

5. Model validation

5.1. Model validation by numerical parameters

Numerically, the computational model must be checked according to some numerical conditions to verify the stability of the solution. These conditions will be imposed on the convective Courant number (which defines the limit for the physical time step, Δt) and the Wall Y+ (which defines the limit for the cell size in the boundaries, Δs).

Several sensitivity analysis of the time step has been performed. The first changing from 0.2 s to 20 s and the second limiting the maximum convective Courant number to 1 in the entire domain by means of a User Defined Function (UDF). In the latter case, the maximum simulated time has been 3600 s because simulation involves time steps much lower than 0.2 s, and therefore higher computational cost, and until that time, time solutions seem identical.

A time step of 2 s (the one here described) supplied the best performance in terms of CPU time and solution independence from the time step value. The maximum convective Courant numbers for the maximum time computed (7050 s) ranges from values lower than 1 in the entire domain out of the SG to maximum values of approximately 873, located in very few cells of the narrowest part of the diffuser.

Great efforts have been made to improve mesh in this part of the diffuser in order to have the smallest possible maximum convective Courant number values, and has been checked that these isolated maximum values have no effect on the global results of the simulation.

Since the K–E model and All Y+ wall treatment have been applied, the values of the Wall Y+ function on all the boundaries should be lower than 150, [26]. For the maximum time computed (7050 s), all surfaces supply a Wall Y+ below 110.

The iteration procedure is assumed to give converged figures every time step by the following two criteria: (1) change in velocity magnitude lower than 10^{-6} m/s at least in 5 iterations at the expected fastest point in the system. This point corresponds to the narrowest part of the SG diffuser. And (2) a maximum number of 50 iterations per time step.

5.2. Model validation by experimental data

Accordingly to the initial and boundary conditions stablished, the following measurements of October, 29th 2012 discharge, [7],

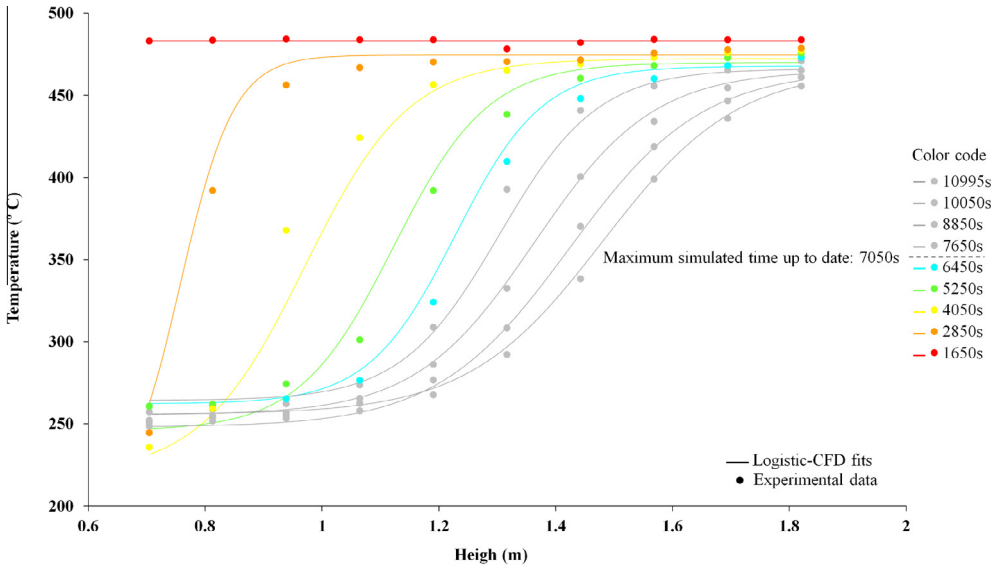

Fig. 6. Helical coil temperature profiles.

Table 3
Characteristic parameters of logistic-CFD functions for each time *t*.

Time (s)	T_{min} (°C)	T_{max} (°C)	H_0 (m)	*s*
2850	194.9	474.5	0.757	0.046
4050	219.3	472.3	0.970	0.089
5250	245.9	470.0	1.122	0.081
6450	262.2	467.8	1.228	0.074
7650	264.2	466.2	1.303	0.084
8850	255.5	465.3	1.363	0.102
10,050	248.1	465.6	1.423	0.114
10,995	255.9	466.8	1.481	0.116

and derived quantities have been used to validate the proposed CFD model:

- MS temperatures below the three helical coils (TI.8.110, Fig. 1),
- Power exchanged between MS and water-steam ($\dot{Q}$), and
- MS mass flow rate across the SG ($\dot{m}_{MS}$).

In Fig. 8, experimental (TI.8.110, in Fig. 1) versus numerical MS temperatures at the bottom of SG are shown.

As can be appreciated the numerical results agree quite well with the experimental data along all the simulation, with a maximum difference of 28 °C in the transient (equivalent to a 7% of percent error) and 10 °C in the steady state (equivalent to a 3% of percent error).

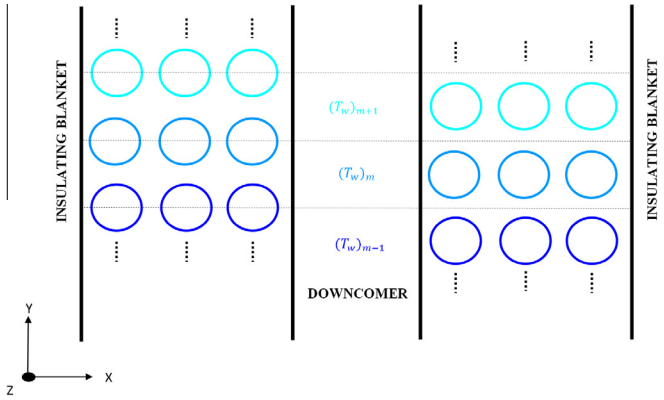

Fig. 7. Boundary condition of the three helical coils based on experimental data.

Experimental water – MS power exchanged ($\dot{Q}$) is a derived quantity that can be calculated using the following expression:

$$\dot{Q} = \dot{m}_{WS}(H_{OUT} - H_{IN})$$

where $\dot{m}_{WS}$ is the experimental water mass flow rate, H_{OUT} and H_{IN} the enthalpies at the outlet (superheated steam) and inlet (saturated water) of the SG respectively, obtained from [27] and evaluated at its corresponding pressure and temperature conditions,

Fig. 9 shows how good the agreement between numerical and experimental results is. Although in the transient the experimental data go almost always below the numerical results (from 2050 s up to 5250 s physical time up to a maximum of 46 kW, equivalent to a 77% of percent error), in the steady state both figures are very close, with a maximum difference of 15 kW, equivalent to an 8% of percent error).

The observed steps in the experimental data are due to the water side management that, by safety reasons, is operated increasing by steps the water flow rate and the pressure until test nominal conditions. These steps are not observed in the numerical results because of the time evolution of the boundary condition have been implemented with smooth transitions.

The experimental MS mass flow rate is also a derived quantity that can be obtained by

$$\dot{m}_{MS} = \frac{\dot{Q}}{\overline{Cp_{MS}}(T_{OUT-}T_{IN})}$$

where $\dot{Q}$ is water – MS power exchanged, T_{OUT} and T_{IN} the temperatures at the outlet and inlet of SG (TI.8.110 and TI.8.111 respectively in Fig. 1), and $\overline{Cp_{MS}}$ the average heat capacity of the Molten Salts between the inlet and the outlet of SG.

In Fig. 10, experimental and numerical results are shown during both the transient and steady states. In the steady state (from 5250 s up to 7050 s physical time), experimental and numerical results are separated no more than 0.08 kg/s, equivalent to a 9% of percent error, while in the transient state, from 2050 s up to 5250 s physical time, experimental and numerical results are separated up to 0.28 kg/s, equivalent to a 60% of percent error.

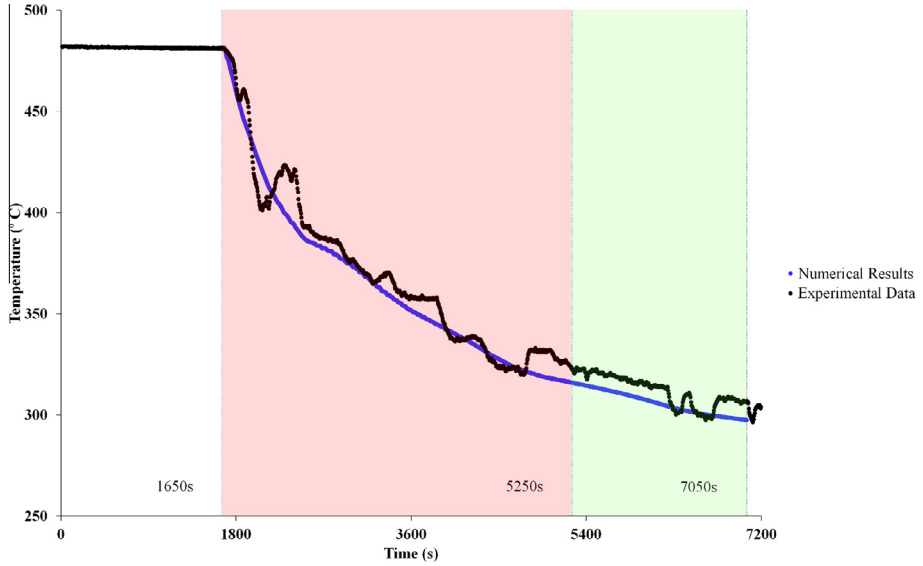

Fig. 8. MS temperatures at the bottom of SG.

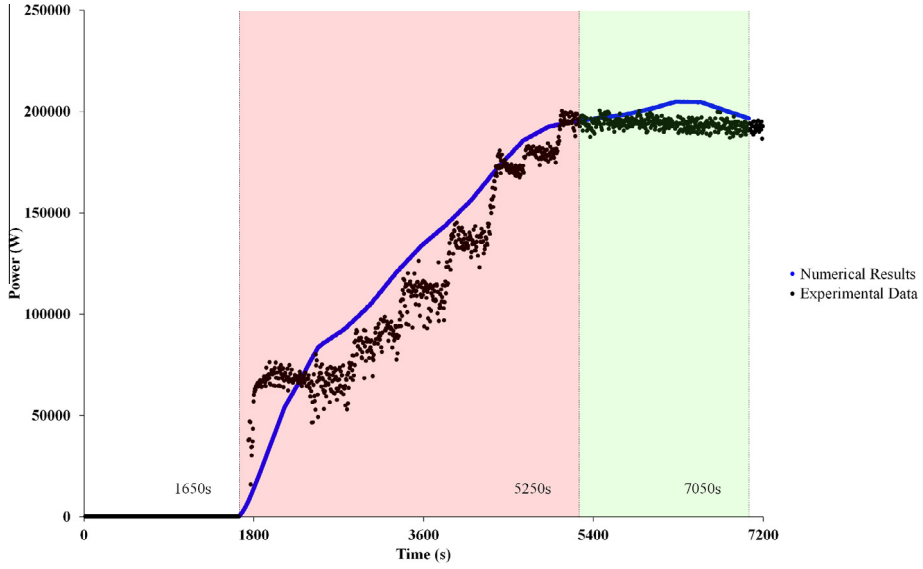

Fig. 9. Power exchanged between MS and water-steam.

As mentioned before, one advantage of erecting a global model that includes not only the Molten Salts circulating through the SG but also the bulk Molten Salts is to have the possibility to validate the model with experimental MS Bulk temperatures (14 thermocouples placed in the thermocouple tree of Fig. 1). In Fig. 11, the experimental versus numerical MS bulk temperatures in different times, 1800 s, 3600 s, 4500 s, 5400 s, are shown. Maximum temperature differences of: 7 °C with the numerical results at 1800 s (equivalent to a 2% of percent error), 21 °C with the numerical results at 3600 s (equivalent to a 5% of percent error), 14 °C with the numerical results at 4500 (equivalent to a 3% of percent error) and 27 °C with the numerical results at 5400 s (equivalent to a 8% of percent error), are observed.

Table 4 summarizes the number of data (N) and the errors of the numerical results ($Num.Result_i$) with respect to the experimental results ($Exp.Result_i$) for the following measurements: TI.8.110, $\dot{Q}$, $\dot{m}_{WS}$, MS bulk T at 1800 s, MS bulk T at 3600 s, MS bulk T at 4500 s and MS bulk T at 5400 s, during both the transient and steady states.

The Mean Absolute Percentage Error (*MAPE*) and Mean Absolute Deviation Percent (*MADP*) indicated in Table 4 are defined in the following manner:

$$MAPE = \frac{\sum_{i=1}^{N} \frac{|Exp.Result_i - Num.Result_i|}{Exp.Result_i}}{N}$$

$$MADP = \frac{\sum_{i=1}^{N} |Exp.Result_i - Num.Result_i|}{\sum_{i=1}^{N} |Exp.Result_i|}$$

6. Local heat transfer coefficients

From the numerical results at 7050 s (steady state) local heat transfer coefficients of MS with the helical coils are calculated.

Setting a local reference system in cylindrical coordinates (r,θ,z) centred at the SG axis (Fig. 12), it has assumed that heat transfer coefficient distributions $h_m(r,\theta,z)$ around the three helical coils are equal between them and along each helical turn m, with

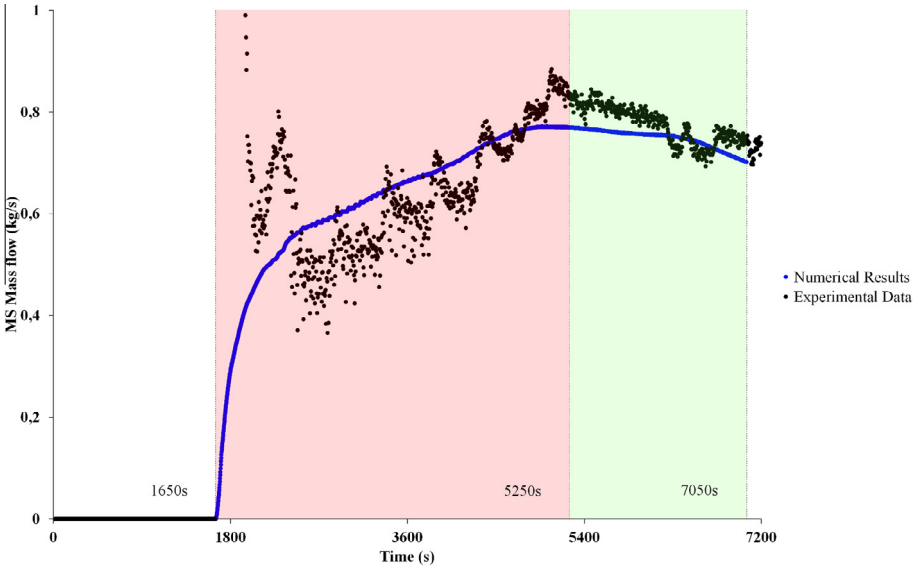

Fig. 10. The MS mass flow rate.

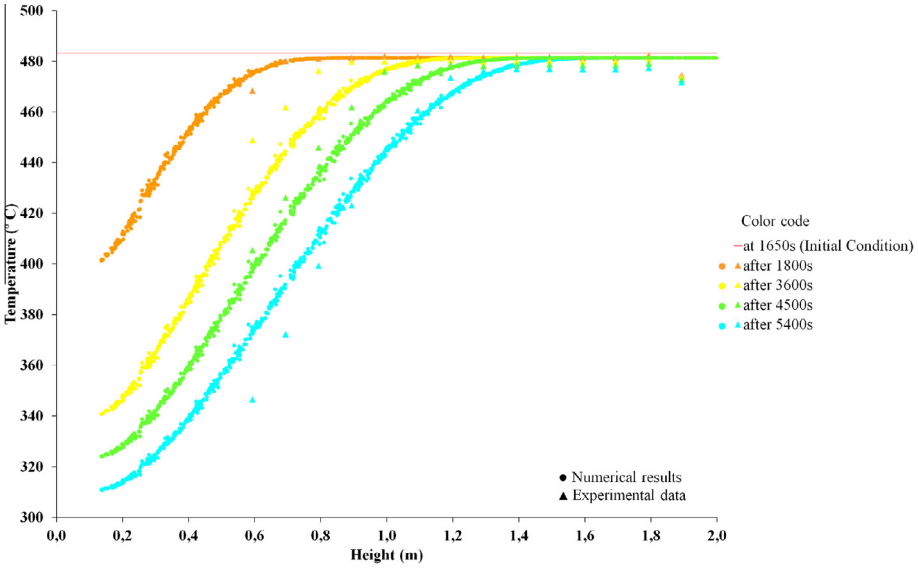

Fig. 11. MS Bulk temperatures.

Table 4
MAPE and MADP for TI.8.110, $\dot{Q}$, $\dot{m}_{WS}$, MS bulk T at 1800 s, MS bulk T at 3600 s, MS bulk T at 4500 s and MS bulk T at 5400 s.

Measurement	N	MAPE	MADP
TI.8.110	541	0.019	0.020
$\dot{Q}$	501	1.000	0.089
$\dot{m}_{WS}$	501	0.100	0.089
MS bulk T at 1800 s	14	0.003	0.003
MS bulk T at 3600 s	14	0.012	0.011
MS bulk T at 4500 s	14	0.013	0.012
MS bulk T at 5400 s	14	0.019	0.017

$m = 1, 2, \ldots, 65$ (i.e. they are periodical with r and independent of θ). Therefore, the following set of surface elements $\Delta S_n = \Delta r \cdot \Delta z$ with $n = 0, 1, \ldots, 9$, uniformly distributed along the SG (Fig. 12) can be taken to obtain the heat transfer coefficient distributions around the helical coils without loss of generality.

The heat transfer coefficient distributions $h_n(r,z)$ with $n = 0, 1, \ldots, 9$, have been calculated by means of $\dot{Q}_n(r,z)/(T_\infty - T_w)_n$, where $\dot{Q}_n(r,z)$ are the numerical heat fluxes around the coils and $(T_\infty - T_w)_n$ the differences between MS bulk and wall of the coils temperatures, in each ΔS_n. The T_∞ in each ΔS_n is the numerical temperature of the MS bulk before facing the coils (red dot in Fig. 12). The surface elements ΔS_n considered for these calculations are so that they are at the same temperature, $(T_w)_n$ (Fig. 12). The T_w in each ΔS_n is the boundary condition of the three helical coils based on experimental data (Fig. 7).

In Fig. 13 the heat transfer coefficient distribution for the surface element ΔS_5 is shown as example, since the qualitative behaviour is repeated for every ΔS_n. These data, $h_5(r,z)$, have been calculated as it is explained in the previous paragraph. As expected, different behaviour is observed when looking at the top and bottom parts of the helical coils (pipe areas intersecting 1 and 4 in pink at Fig. 12) and at the surfaces facing the narrowest conduit between coils (pipe areas intersecting 2 and 3 in pink at Fig. 12).

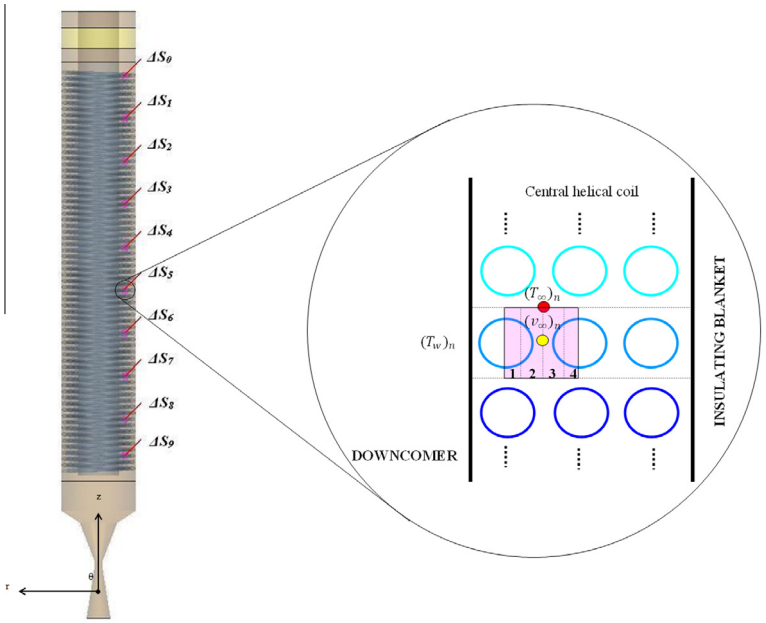

Fig. 12. (a) Surface elements considered for local heat transfer coefficient calculations, (b) helical turn *n*. (For interpretation of the references to colour in this figure legend, the reader is referred to the web version of this article.)

The obtained heat transfer coefficients in all elements ΔS_n are comprised between 600 and 1200 W/m^{2}K. The maximum values are associated to the narrowest conduit between coils (areas 2 and 3 at Fig. 12) and the minimum to the top and bottom parts of the helical pipes (areas 1 and 4 at Fig. 12). For given a radial position r, the highest values of the heat transfer coefficients correspond to the top parts of the helical coils.

A local heat transfer coefficient $\overline{h_n}$ for every surface element ΔS_n has been calculated by surface averaging of the scalar distributions $h_n(r,z)$ on each surface ΔS_n. The software carries out these averages by means of,

$$\overline{h_n} = \frac{1}{S_n}\int_n^h (r,z)dS_n \tag{1}$$

In Fig. 14 these coefficients in the set surface elements ΔS_n are shown.

The obtained local heat transfer coefficients are comprised between 775 W/m^{2}K at the bottom of the SG (at ΔS_9) and 950 W/m^{2}K at its nearly top (at ΔS_1). Local heat transfer coefficient trend with the SG height is quite different between bottom and top parts: while at the bottom they maintain almost constant (dashed line), from a determined SG height (between ΔS_7 and ΔS_6) the local heat transfer coefficients increase linearly (solid line). This is due to the temperature profiles assumed as boundary condition.

It is noted that the local heat transfer coefficient at the upper part of the SG, $\overline{h_0}$, presents a value far from the top linear trend. This maybe because the first helical turn faces the MS just after they have passed thought opening of the SG, which is perpendicular to the main MS direction along the SG, so the heat transfer in ΔS_0 maybe not as effective as in the following elements.

7. Shell-side heat transfer correlation

The MS flowing through the SG by natural convection also experiment other induced accelerations due to the proximity of the three helical coils. These accelerations certainly improve the convective heat transfer between MS at coils.

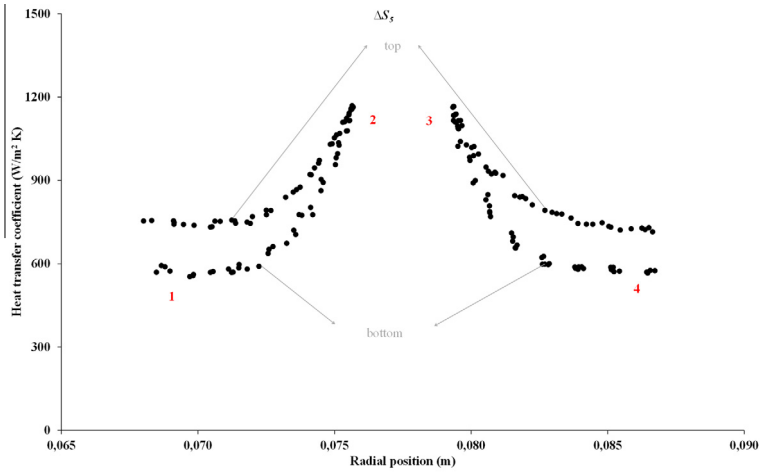

Fig. 13. Heat transfer coefficient distribution around the surface element ΔS_5.

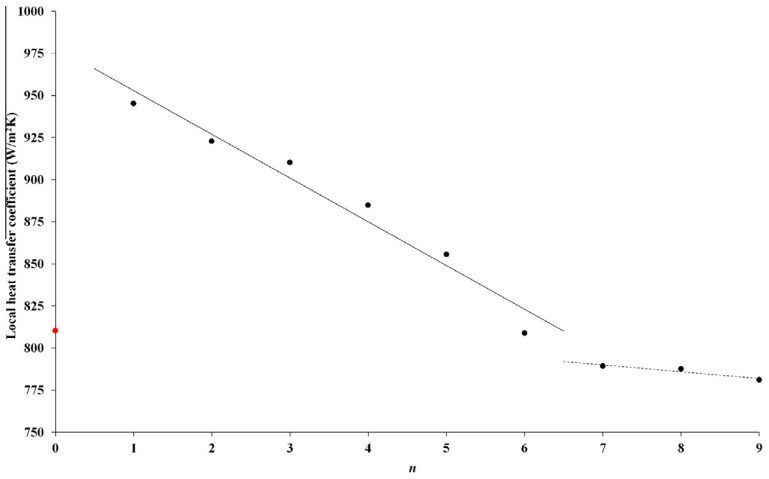

Fig. 14. Local heat transfer coefficients along the SG.

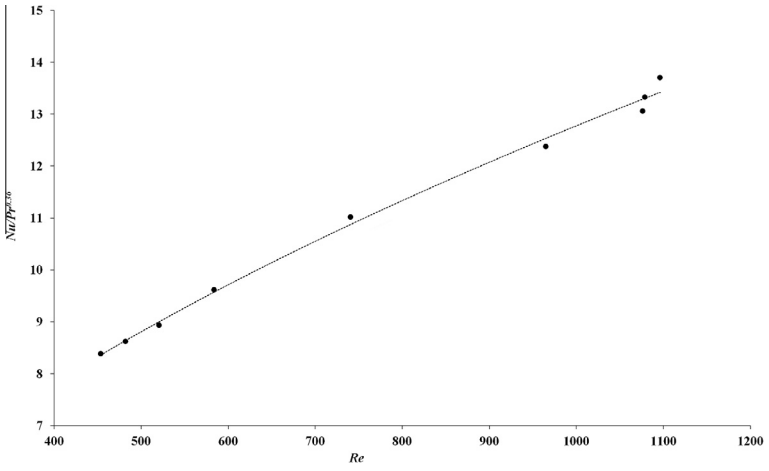

Fig. 15. Fit of the heat transfer data.

Therefore, it is proposed to treat the heat transfer of MS to helical coils as an indirect forced convection phenomenon, so the corresponding Nusselt number, *Nu*, can be expressed by:

$$Nu = Nu(Re, Pr)$$

where *Re* and *Pr* represent the Reynolds and Prandtl numbers, respectively.

For single-phase flows in ducts, over objects or matrix, experimental results for forced convection used to be correlated by expressions of type:

$$Nu = cRe^{a}Pr^{b}$$

where c, a and b are constants that depend on the geometry, [28].

This form of correlation has been used in this paper, where, the Nusselt (*Nu*), Reynolds (*Re*) and Prandtl (*Pr*) numbers are based on the outer diameter of the helical coils (d_0), the local heat transfer coefficients calculated in the previous paragraph ($\overline{h_n}$), the maximum numerical velocities close to the pipes (i.e. the velocities in the centre of the conduit between pipes, $(v_\infty)_n$, Fig. 12) and the MS physical properties (κ, ρ, Cp and μ) calculated at a temperature $\left(\frac{T_\infty + T_w}{2}\right)_n$, Fig. 12.

The values of c and a of the equation have been determined by a minimum squares fit of the heat transfer data (Fig. 15), while the value b has been prefixed at 0.36, as in the extensive works on normal cross flow for inline and staggered tube bundle geometries by Zukauskas and Ulinskas, [29], and Zukauskas, [30], comprising *Re* between 1 and 200,000. For this adjustment the value of $\overline{h_0}$ has not been considered, due to its uneven behaviour for being evaluated so close to the SG inlet.

With a statistical parameter of the fitting, R^2, of 0.996, the following correlation for the shell-side has been found,

$$Nu = 0.3146Re^{0.54}Pr^{0.36}$$

This correlation is valid for the conditions here considered, i.e., for ranges of *Re* between 400 up to 1200, *Pr* between 4 up to 11, an average winding angle of 2° and an outer diameter of the helical coils of 0.0127 m.

Note that variations in Reynolds number are not caused by velocity variations within the SG but by the MS property variations due to the temperature changes within the SG. While velocities go from a minimum of 0.066 m/s up to a maximum of 0.070 m/s, the ratios $\left(\frac{\rho}{\mu}\right)$ go from 514,243 s/m^2 up to 1,297,257 s/m^2.

Finally, a comparison between correlations mentioned in Table 1 for different *Re*, taking *Pr* = 7.5 value (average value *Pr* = 4–11), is shown in Fig. 16.

Messa et al., (2) correlation, although it has been validated up to $Pr \sim 7.8$, gives *Nu* values for this specific case below the ones obtained by the simulation already explained. This maybe explain

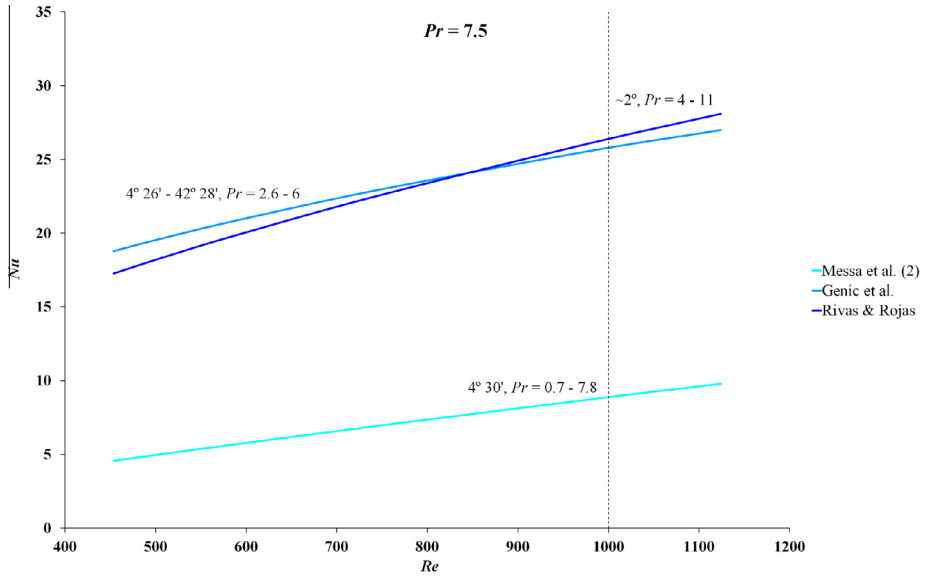

Fig. 16. Comparison of heat transfer correlations for MS. Close to lines the winding angles and *Pr* number to which the correlations are valid are given.

when considering that the heat exchanger configuration for which the correlation was validated is less effective in transferring heat that the SG configuration of this case: d_0 is lower than 0.0127 m (0.0064 m), vertical and horizontal pitch are higher than 0.018 m and 0.016 m (0.026 m and 0.026 m) and the coil configuration is not inline (staggered).

With the Genic et al. correlation, [5], although validated for $Pr = 6$ and $d_h = 0.0183$ m (in this specific configuration $d_h = 0.0130$ m), *Nu* trends with *Re* very similar to the correlation here proposed, with a maximum difference of 8% (Fig. 16).

8. Conclusions

A new heat transfer correlation for MS appropriate for helical-coil tube bundles with OPTS SG's configuration is proposed. The correlations found in the literature are not useful because, either they are not suitable for MS or the SG design is different enough to influence the corresponding heat transfer coefficients.

In order to obtain the correlation, a Computational Fluid Dynamic (CFD) model of the 300kW$_{th}$ MS prototype erected in the Casaccia Research Centre of ENEA (Italy) has been carried out, which has been validated with the experimental data obtained during one of its discharge tests.

From numerical results of CFD model at the steady state (which show an agreement with the experimental results in a range between a 3% and a 9% of percent error), the MS velocities, temperatures and wall heat fluxes within the SG have been obtained. A methodology for calculating the local heat transfer coefficients along the SG is proposed using the already mentioned variables. The obtained coefficients are comprised between 775 W/m^{2}K at the bottom of the SG and 950 W/m^{2}K at its top.

The proposed correlation in dimensionless form is: $Nu = 0.3146 Re^{0.54} Pr^{0.36}$, where *Re* and *Nu* are based on the outer diameter of the helical coils. The correlation is valid for ranges of *Re* between 400 up to 1200, *Pr* numbers between 4 to 11, and average winding angle of 2° and an outer diameter of the helical coils of 0.0127 m. It achieves an accurate fit to the numerical results with a statistical parameter R^2 of 0.996.

Conflict of interest

None declared.

Acknowledgments

The authors would like to acknowledge the E. U. through the 7th Framework Programme for the financial support of this work under the O.P.T.S. project with contract number: 283138 and to the UTRINN-STD from Casaccia for providing the experimental data and the information concerning to the experimental setup.

References

[1] Program on Technology Innovation: Evaluation of Concentrating Solar Thermal Energy Storage Systems, EPRI, Palo Alto-California, 2009
[2] U. Herrmann, D. Kearney, Survey of thermal energy storage for parabolic trough power plants, J. Sol. Energy Eng. 124 (2002) 145–152, http://dx.doi.org/10.1115/1.1467601.
[3] J. Messa, S. Foust, W. Poehlein, Shell-side heat transfer coefficients in helical coil heat exchangers, Ind. Eng. Chem. Process Des. Develop. 8 (3) (1969) 343–347, http://dx.doi.org/10.1021/i260031a008.
[4] E.M. Smith, Advanced in thermal design of heat exchangers, A Numerical Approach: Direct-Sizing, Step-Wise Rating, and Transients, Wiley, Chichester, 2006, ISBN 978-0470016169.
[5] S. Genic, B. Jacimovic, M. Jaric, N. Budimir, M. Dobrnjac, Research on the shell-side thermal performances of heat exchangers with helical tube coils, Int. J. Heat Mass Transfer 55 (15–16) (2012) 4295–4300, http://dx.doi.org/10.1016/j.ijheatmasstransfer.2012.03.074.
[6] M. Ahmed, Unsteady numerical simulation for studying the thermocline phenomenon inside a storage tank for molten salt, J. Appl. Sci. Res. 8 (8) (2012) 4635–4644 (ISSN: 1819-544X).
[7] E. Rivas, E. Rojas, Experimental data analysis of the tank storage prototype with an integrated 300kW steam generator, OPTS Project Report, OPTS-TE-MI-01, CIEMAT-PSA, Madrid, July 2014 .
[8] STAR-CCM+ Version 8.04.010® User Guide, CD-adapco. (Only accessible by registry).
[9] L. Rinaldi, F. Fabrizi, A. Alemberti, W. Gaggioli, S. Aliotta, A. Barbensi, P. Tarquini, International application published under the patent cooperation treaty (PCT). International Publication Number WO 2012/080970 A2, 2012.
[10] F. Fabrizi, L. Rinaldi, A. Petroni, C. Rocca, Placement of instrumentation in the 300kW SG test section, Drawing of Progetto solare termodinamico, Impianto prova collettori solari (P.C.S.), ENEA, Centro Ricerche Casaccia, Roma, July 2012.
[11] I. Demirdzic, S. Musaferija, Numerical method for coupled fluid flow, heat transfer and stress analysis using unstructured moving meshes with cells of arbitrary topology, Comput. Methods Appl. Mech. Eng. 125 (1–4) (1995) 235–255, http://dx.doi.org/10.1016/0045-7825(95)00800-G.
[12] J. Ferziger, M. Peric, Computational Methods for Fluid Dynamics, third rev. ed., Springer-Verlag, Berlin, 2002, ISBN 978-3-642-56026-2.
[13] S. Mathur, J. Murthy, Pressure-based method for unstructured meshes, Numer. Heat Transfer, Part B: Fundam. Int. J. Comput. Method. 31 (2) (1997) 195–215, http://dx.doi.org/10.1080/10407799708915105.
[14] S. Mathur, J. Murthy, Pressure boundary conditions for incompressible flow using unstructured meshes, Numer. Heat Transfer, Part B: Fundam. Int. J. Comput. Method. 32 (3) (1997) 283–298, http://dx.doi.org/10.1080/10407799708915010.

[15] M. Peric, R. Kressler, G. Scheuerer, Comparison of finite-volume numerical methods with staggered and colocated grids, Comput. Fluids 16 (4) (1988) 389–403, http://dx.doi.org/10.1016/0045-7930(88)90024-2.
[16] I. Demirdzic, Z. Lilek, M. Peric, A collocated finite volume method for predicting flows at all speeds, Int. J. Numer. Methods Fluids 16 (12) (1993) 1029–1050, http://dx.doi.org/10.1002/fld.1650161202.
[17] H. Versteeg, W. Malalasekera, An Introduction to Computational Fluid Dynamics, the Finite Volume Method, Prentice Hall, 2007, ISBN 978-0131274983.
[18] N. Devore, H. Yip, J. Rhee, Domestic hot water storage tank: design and analysis for improving thermal stratification, J. Sol. Energy Eng. 135 (4) (2013) 040905, http://dx.doi.org/10.1115/1.4025517.
[19] A. Abánades, A. Peña, Steady-state natural circulation analysis with computational fluid dynamic codes of a liquid metal-cooled accelerator driven system, Nucl. Eng. Des. 239 (2) (2009) 418–424, http://dx.doi.org/10.1016/j.nucengdes.2008.10.028.
[20] B. Hazim, Calculation of convective heat transfer coefficients of room surfaces for natural convection, Energy Build. 28 (2) (1998) 219–227, http://dx.doi.org/10.1016/S0378-7788(98)00022-X.
[21] W. Xu, Q. Chen, F.T.M. Nieuwstadt, A new turbulence model for near wall natural convection, Int. J. Heat Mass Transfer 41 (21) (1998) 3161–3176, http://dx.doi.org/10.1016/S0017-9310(98)00081-7.
[22] M. Jischa, H. Rieke, About the prediction of turbulent Prandtl and Schmidt numbers from modelled transport equations, Int. J. Heat Mass Transfer 22 (11) (1979) 1547–1555, http://dx.doi.org/10.1016/0017-9310(79)90134-0.
[23] S. Churchill, A reinterpretation of the turbulent Prandtl number, Ind. Eng. Chem. Res. 41 (25) (2002) 6393–6401, http://dx.doi.org/10.1021/ie011021k.
[24] R. Bradshaw, R. Carling, A review of the chemical and physical properties of molten alkali nitrate salts and their effect on materials used for solar central receivers, SAND87-8005/ON: DE88010500, Sandia National Laboratories, Livermore-California, 1987.
[25] R. Ferri, A. Cammi, D. Mazzei, Molten salt mixture properties in RELAP5 code for thermodynamic solar applications, Int. J. Therm. Sci. 47 (12) (2008) 1676–1687, http://dx.doi.org/10.1016/j.ijthermalsci.2008.01.007.
[26] <http://www.cd-adapco.com/engineering-technical-support> (available by login).
[27] W. Wagner, A. Kruse, Properties of Water and Steam: The Industrial Standard IAPWS-IF97 for the Thermodynamic Properties and Supplementary Equations for Other Properties, Springer, Berlin, 1998, ISBN 978-3540643395.
[28] F. Kreith, R. Manglik, M. Bohn, Principles of Heat Transfer, seventh ed., Cengage Learning, 2010, ISBN 978-0495667704.
[29] A.A. Zhukauskas, A. Zukauskas, R. Ulinskas, Heat transfer in tube banks in cross flow, Hemisphere Publishing Corporation, 1988, ISBN 978-0891166856.
[30] A. Zukauskas, Convective heat transfer in cross flow, in: S. Kakaç, R.K. Shah, W. Aung (Eds.), Handbook of Single-Phase Convective Heat Transfer, John Wiley & Sons Inc., 1987, ISBN 978-0471817024.
[31] S. He, J. Lu, J. Ding, T. Yu, Y. Yuan, Convective heat transfer of molten salt outside the tube bundle of heat exchanger, Exp. Thermal Fluid Sci. 59 (2014) 9–14, http://dx.doi.org/10.1016/j.expthermflusci.2014.07.008.